Journal of Loss Prevention in the Process Industries 77 (2022) 104761

Contents lists available at ScienceDirect

Journal of Loss Prevention in the Process Industries

journal homepage: www.elsevier.com/locate/jlp

Numerical study of premixed gas explosion in a 1-m channel partly filled with 18650 cell-like cylinders with experiments

M. Henriksen [a,*], K. Vaagsaether [a], J. Lundberg [a], S. Forseth [b], D. Bjerketvedt [a]

[a] Faculty of Technology, Natural Sciences and Maritime Sciences, University of South-Eastern Norway, Kjølnes Ring 56, Porsgrunn, 3901, Norway
[b] Norwegian Defence Research Establishment (FFI), Oslo, Norway

ARTICLE INFO

Keywords:
Li-ion battery safety
Open-source software
OpenFOAM
Explosion simulation
Premixed combustion

ABSTRACT

Abused and defective Li-ion cells can cause a catastrophic failure of a Li-ion battery (LIB), leading to severe fires and explosions. In recent years, several numerical and experimental studies have been conducted on the explosion hazard related to the vented combustible gases from failed Li-ion cells. Experimentally quantifying fundamental properties for failing LIBs is essential for understanding safety issues; however, it can be costly, time-consuming, and can be partly incomplete. Computational fluid dynamic (CFD) simulations have been an essential tool for studying the risk and consequences in the process industry. In this study, the prediction accuracy of the open-source CFD combustion model/solver XiFoam was evaluated by comparing numerical simulations and experiments of premixed gas explosions in a 1-m explosion channel partly filled with 18650 cell-like cylinders. The prediction accuracy was determined by calculating the mean geometric bias and variance for the temporal pressure evolution, maximum pressure peak, positive impulse, spatial flame front velocity for two different channel geometries, in addition to two gas compositions at several fuel-air equivalence ratios. From this method, the XiFoam model/solver gave an overall acceptable model performance for both geometries and gas composition.

1. Introduction

Over the last decade, several fires and explosions have been caused by failing Li-ion batteries (LIBs). For example, in Texas, USA, in April 2017, a train car carrying discarded LIBs for recycling caused an explosion, which shattered windows 350 feet from the incident (Sophia Beausoleil, 2017). In April 2019, a Li-ion battery energy storage system (BESS) caught fire in Arizona, USA. Three hours after the fire suppressant had extinguished the fire, firefighters entered the BESS, shortly after that, an explosion occurred. The BESS was severely damaged, and several firefighters were injured (Hill, 2020). Similarly, in September 2020, there was a fire in a 20 MWh BESS in Liverpool, UK. The BESS was already well alight when the firefighters arrived, and residents in the vicinity reported hearing an explosion (Andy Colthorpe, 2020; Ben Turner, 2020). In April 2021, a fire occurred in a solar panel installation with 25 MWh of lithium-iron-phosphate (LFP) LIB on the rooftop of a shopping mall in Beijing, China. While the firefighters tried to extinguish the fire, an explosion occurred. The explosion led to the death of two firefighters. Due to limiting accidental information, the definite cause of the explosion is not known (CTIF - International Association of Fire and Rescue Services, 2021).

If Li-ion cells are over-charged, over-discharged, short-circuited, deformed, punctured, or exposed to heat, there is a possibility for a catastrophic failure (Lian et al., 2019; Mikolajczak et al., 2011; Wang et al., 2019). A failing LIB can release gases such as hydrogen (H_2), carbon monoxide (CO), carbon dioxide (CO_2), methane (CH_4), electrolyte solvents, and toxic species (Fernandes et al., 2018; Golubkov et al., 2014, 2015; Lammer et al., 2017; Nedjalkov et al., 2016; Roth et al., 2004; Somandepalli et al., 2014; Wang et al., 2019). When combustible gases mix with air, they can cause explosions and fires (Bjerketvedt et al., 1997).

In recent years, researchers have experimentally and numerically investigated the explosion hazard abused LIBs pose by determining the released gas composition, gas release rates, and combustion properties of the gas vented (Wang et al., 2019; Fernandes et al., 2018; Johnsplass et al., 2017; Henriksen et al., 2019, 2020; Baird et al., 2020; M. Henriksen et al., 2021; Kennedy et al., 2021). Fernandes et al. (2018) determined the gas composition and total amount of released gas from commercial Li-ion cells abused by overcharge. The study showed that the abused cells mainly released electrolyte solvent, along with

* Corresponding author.
E-mail address: mathias.henriksen@usn.no (M. Henriksen).

https://doi.org/10.1016/j.jlp.2022.104761
Received 19 August 2021; Received in revised form 14 February 2022; Accepted 28 February 2022
Available online 22 March 2022

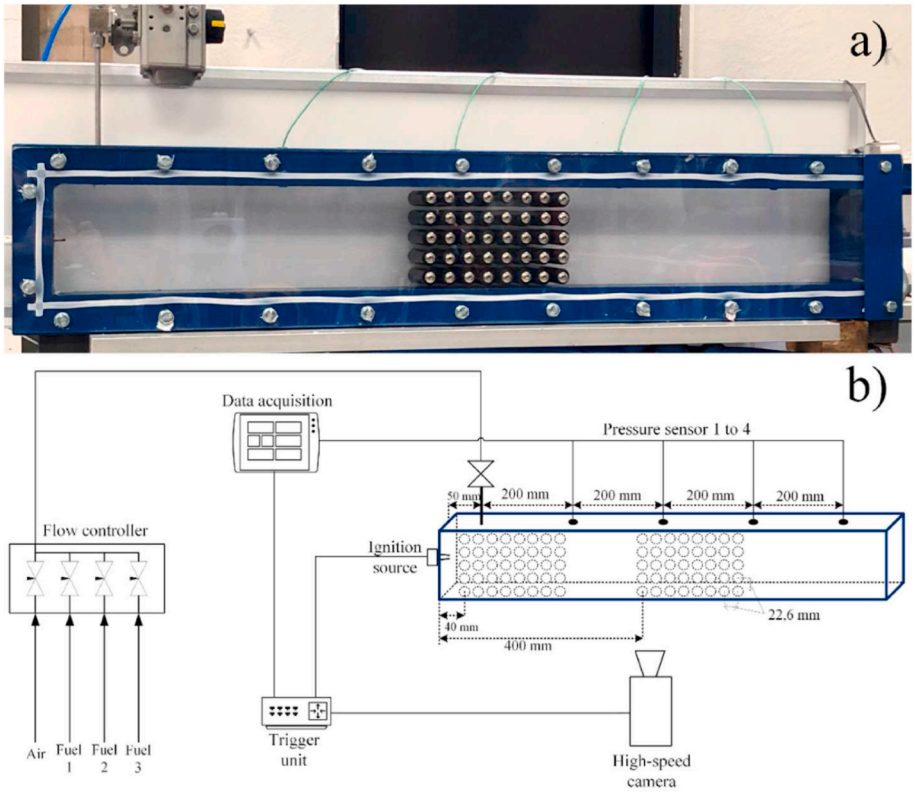

Fig. 1. Photo and schematic illustration of the 1-m explosion channel. a): Photo of explosion channel with the Li-ion 18650 cell-like cylinders in the center of the channel; b): Schematic illustration of the experimental setup with dimensions.

Table 1
The gas compositions analyzed numerically and experimentally in this study in volume percentage.

Name of fuel mixture	H_2 [%]	CO [%]	CO_2 [%]	CH_4 [%]	C_2H_4 [%]
High LBV Li-ion gas	42.8	37.1	10.0	7.1	3.0
Simplified Li-ion gas	35.0	[-]	[-]	65.0	[-]

hydrogen and other hydrocarbons. Henriksen et al. (Henriksen et al., 2019, 2020) experimentally determined the explosion characteristics of several Li-ion electrolyte solvents and the laminar burning velocity (LBV) for the solvent dimethyl carbonate (DMC). The Li-ion electrolyte solvents had similar explosion characteristics as propane, whereas DMC had a slightly lower LBV than propane.

Moreover, Baird et al. (2020) numerically estimated the lower explosive limit, explosion pressure, rate of explosion pressure rise, and the LBV for various vented Li-ion gas compositions found in the literature. The study showed that LBV ranged from 0.3 m/s to 1.1 m/s, depending on the state of charge (SOC) and cell chemistry. Kennedy et al. (2021) studied the release rates, total volume released, and gas composition from a single cell to an array of five and ten cells. The study showed that the venting speed, the total amount of gas released, and cell to cell propagation increased as the SOC increased. For a more compressive literature study, we suggest the articles by Fernandes et al. (2018), Wang et al. (2019), and Baird et al. (2020).

Experimentally quantifying fundamental properties for failing LIBs is essential for understanding safety issues; however, it can be costly and time-consuming and can be partly incomplete. Computational fluid dynamics (CFD) simulations have become essential for evaluating explosion consequences and risks, especially in the process industry (Diakow et al., 2018; Hansen et al., 2010; Hansen and Middha, 2008; Shen et al., 2020). Using CFD tools such as FLACS, OpenFOAM, and ANSYS Fluent to predict explosion pressures, blast loads (impulse), and gas dispersion can significantly improve the safety of a design. Most CFD simulations related to LIBs are on single-cell failure, single-cell thermal runaway characterization, and cell-to-cell propagation (Kim et al., 2007, 2021; Srinivasan et al., 2020). In a report by DNV GL (Helgesen, 2019), the LIB explosion hazard was investigated by CFD simulations of gas dispersion and gas explosions in maritime LIB installations. DNV GL reported explosion pressures between 90 kPa (gauge) and 270 kPa (gauge) in a partly confined geometry depending on the Li-ion gas release profile.

The benefits from simulations are heavily dependent on the prediction accuracy of the CFD models. Therefore, this study explores the prediction accuracy of the XiFoam combustion model/solver in the open-source CFD toolbox OpenFOAM (CFD Direct, 2021; H. G. Weller et al., 1998). More specifically, we analyze prediction accuracy of the temporal evolution of the pressure, maximum pressure peak, positive impulse, and the spatial evolution of the flame front for two gas compositions in a 1-m-long explosion channel, partly filled with 18650 cell-like cylinders. In addition, two different channel geometries were studied by varying the location of an identical set of 40 18650 cell-like cylinders. The prediction accuracy with an early-onset for turbulent flame propagation was investigated with the cylinders close to the ignitions source. Whereas with the cylinders in the center, i.e., further away from the ignition source, the prediction accuracy with an initial laminar flame propagation stage could be examined.

Finally, in addition to two gas compositions and the two geometries, the CFD simulations were compared at three different fuel-air equivalence ratios (φ) 0.8, 1.0, and 1.2, resulting in a total of 12 simulation cases. The numerical and experimental condition was typical atmospheric conditions, 293 K and 101.3 kPa (absolute).

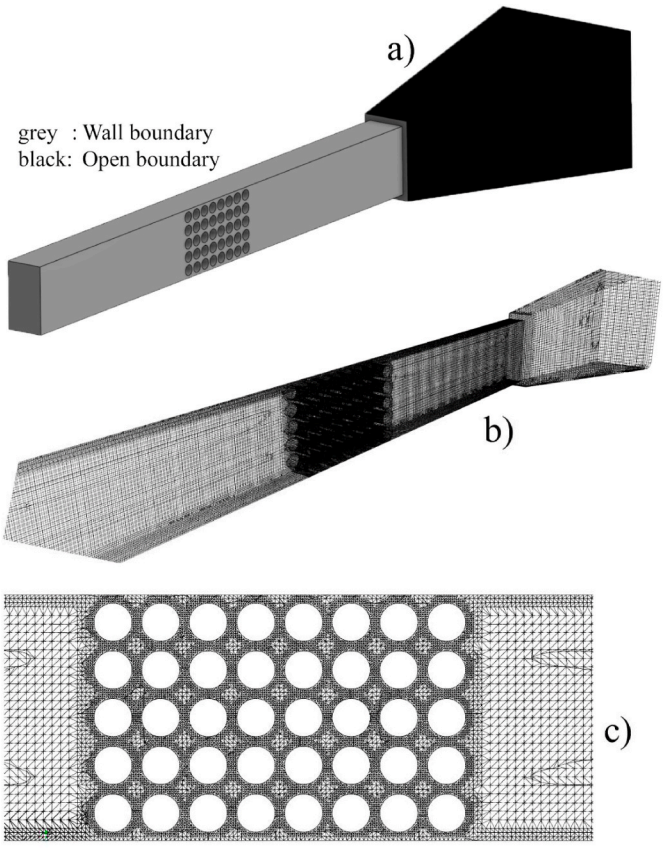

Fig. 2. Images of the geometry and computational mesh used in numerical simulations. a) Side view of the entire CAD geometry with boundary conditions. b) Side view of the computational mesh. c) Horizontal cross-section view of the computational mesh cell geometry.

Table 2
List of variables with the applied wall and open boundary conditions.

Variable	Wall boundary	Open boundary
Temperature (T)	Adiabatic walls (zero gradient) (293 K)	Zero gradient outlet fixed value inlet (T = 293)
Temperature unburnt (T_u)	Adiabatic walls (zero gradient) (293 K)	Zero gradient outlet fixed value inlet (T_u) = 293)
Pressure (p)	Zero gradient at the wall	A constant total pressure, dynamic + static pressure equals 101.3 kPa.
Velocity (U)	Zero velocity at the wall (noSlip)	Zero gradient outlet; inlet value based on flux normal to the boundary surface
LBV (S_u)	Zero gradient at the wall	Zero gradient at the boundary surface
Subgrid turbulent kinetic energy (k)	Zero gradient at the wall	Zero gradient at the boundary surface
Turbulent, LBV ratio (Xi)	Zero gradient at the wall	Zero gradient at the boundary surface
regress variable (b)	Zero gradient at the wall	Zero gradient at the boundary surface
Fuel mixture fraction (ft)	Zero gradient at wall	Zero gradient outlet fixed value inlet (ft = 0)
Turbulent viscosity (nut)	Calculated based on the turbulent kinetic energy	Calculated based on the turbulent properties
Turbulent thermal diffusivity (alphat)	Calculated based on the turbulent viscosity for compressible flow	Calculated based on the turbulent viscosity

Table 3
List of all experiments with the corresponding CFD simulations.

Experiment case number	Gas composition	Fuel-Air Equivalence ratio (φ)	Channel geometry	CFD case name
Case 01.	High LBV Li-ion gas	0.79	Inner	High CFD 0.8 Inner
Case 02.	High LBV Li-ion gas	0.89	Inner	None
Case 03.	High LBV Li-ion gas	1.00	Inner	High CFD 1.0 Inner
Case 04.	High LBV Li-ion gas	1.09	Inner	None
Case 05.	High LBV Li-ion gas	1.18	Inner	High CFD 1.2 Inner
Case 06.	High LBV Li-ion gas	1.18	Inner	High CFD 1.2 Inner
Case 07.	High LBV Li-ion gas	1.29	Inner	None
Case 08.	High LBV Li-ion gas	1.29	Inner	None
Case 09.	High LBV Li-ion gas	1.38	Inner	None
Case 10.	High LBV Li-ion gas	1.38	Inner	None
Case 11.	High LBV Li-ion gas	1.47	Inner	None
Case 12.	High LBV Li-ion gas	1.47	Inner	None
Case 13.	Simplified Li-ion gas	0.69	Inner	None
Case 14.	Simplified Li-ion gas	0.69	Inner	None
Case 15.	Simplified Li-ion gas	0.79	Inner	Simple CFD 0.8 Inner
Case 16.	Simplified Li-ion gas	0.79	Inner	Simple CFD 0.8 Inner
Case 17.	Simplified Li-ion gas	0.90	Inner	None
Case 18.	Simplified Li-ion gas	0.90	Inner	None
Case 19.	Simplified Li-ion gas	0.90	Inner	None
Case 20.	Simplified Li-ion gas	0.97	Inner	Simple CFD 1.0 Inner
Case 21	Simplified Li-ion gas	0.97	Inner	Simple CFD 1.0 Inner
Case 22.	Simplified Li-ion gas	1.01	Inner	Simple CFD 1.0 Inner
Case 23.	Simplified Li-ion gas	1.01	Inner	Simple CFD 1.0 Inner
Case 24.	Simplified Li-ion gas	1.08	Inner	None
Case 25.	Simplified Li-ion gas	1.10	Inner	None
Case 26.	Simplified Li-ion gas	1.10	Inner	None
Case 27.	Simplified Li-ion gas	1.19	Inner	Simple CFD 1.2 Inner
Case 28.	Simplified Li-ion gas	1.19	Inner	Simple CFD 1.2 Inner
Case 29.	Simplified Li-ion gas	1.26	Inner	None
Case 30.	Simplified Li-ion gas	1.29	Inner	None
Case 31.	Simplified Li-ion gas	1.37	Inner	None
Case 32.	Simplified Li-ion gas	1.39	Inner	None

(*continued on next page*)

Table 3 (*continued*)

Experiment case number	Gas composition	Fuel-Air Equivalence ratio (φ)	Channel geometry	CFD case name
Case 33.	High LBV Li-ion gas	0.79	Center	High CFD 0.8 Center
Case 34.	High LBV Li-ion gas	0.89	Center	None
Case 35.	High LBV Li-ion gas	0.89	Center	None
Case 36.	High LBV Li-ion gas	0.97	Center	High CFD 1.0 Center
Case 37.	High LBV Li-ion gas	0.98	Center	High CFD 1.0 Center
Case 38.	High LBV Li-ion gas	0.98	Center	High CFD 1.0 Center
Case 39.	High LBV Li-ion gas	1.08	Center	None
Case 40.	High LBV Li-ion gas	1.09	Center	None
Case 41.	High LBV Li-ion gas	1.09	Center	None
Case 42.	High LBV Li-ion gas	1.18	Center	High CFD 1.2 Center
Case 43.	High LBV Li-ion gas	1.18	Center	High CFD 1.2 Center
Case 44.	High LBV Li-ion gas	1.29	Center	None
Case 45.	High LBV Li-ion gas	1.29	Center	None
Case 46.	High LBV Li-ion gas	1.38	Center	None
Case 47.	High LBV Li-ion gas	1.38	Center	None
Case 48.	High LBV Li-ion gas	1.47	Center	None
Case 49.	High LBV Li-ion gas	1.47	Center	None
Case 50.	Simplified Li-ion gas	0.69	Center	None
Case 51.	Simplified Li-ion gas	0.69	Center	None
Case 52.	Simplified Li-ion gas	0.79	Center	Simple CFD 0.8 Center
Case 53.	Simplified Li-ion gas	0.79	Center	Simple CFD 0.8 Center
Case 54.	Simplified Li-ion gas	0.79	Center	Simple CFD 0.8 Center
Case 55.	Simplified Li-ion gas	0.90	Center	None
Case 56.	Simplified Li-ion gas	0.90	Center	None
Case 57.	Simplified Li-ion gas	1.01	Center	Simple CFD 1.0 Center
Case 58.	Simplified Li-ion gas	1.01	Center	Simple CFD 1.0 Center
Case 59.	Simplified Li-ion gas	1.10	Center	None
Case 60.	Simplified Li-ion gas	1.10	Center	None
Case 61.	Simplified Li-ion gas	1.10	Center	None
Case 62.	Simplified Li-ion gas	1.19	Center	Simple CFD 1.2 Center
Case 63.	Simplified Li-ion gas	1.19	Center	None
Case 64.	Simplified Li-ion gas	1.19	Center	None
Case 65.	Simplified Li-ion gas	1.26	Center	None
Case 66.	Simplified Li-ion gas	1.26	Center	None
Case 67.	Simplified Li-ion gas	1.26	Center	None
Case 68.	Simplified Li-ion gas	1.37	Center	None
Case 69.	Simplified Li-ion gas	1.37	Center	None
Case 70.	Simplified Li-ion gas	1.37	Center	None

2. Materials and methods

2.1. Experimental setup

The explosion channel's length, width, and height are 1000.0 mm, 65.0 mm, and 116.5 mm, respectively. Two different channel setups were analyzed. The channel setup referred to as the inner channel geometry had 40 18650 cell-like cylinders near the closed end of the channel, whereas the channel setup referred to as the center channel geometry had 40 18650 cell-like cylinders approximately in the center of the channel. Each cylinder has a diameter of 18 mm and a length of 650 mm, the same dimensions as a 18650 Li-ion cell. Furthermore, the distance between the cells in the vertical and horizontal direction is 4.6 mm ($\pm$0.1 mm), creating a 0.5 void ratio and maximum blockage ratio of 0.77 in the obstructed part of the channel. For the inner channel geometry, the center of the first column of cylinders was 40 mm from the closed end of the channel. The center of the first column of cells was 400 mm from the closed end of the channel for the center channel geometry. Fig. 1 a) shows a photo of the explosion channel with the center channel geometry, and Fig. 1 b) shows a schematic illustration of the experimental setup with dimensions.

The premixed fuel-air inlet is located 50 mm from the closed end of the channel. With a porous lid attached to the open end of the channel, the channel's volume was exchanged eight times to ensure a homogenous mixture. After filling, there was a 1-min delay before ignition to reduce convective flow. Moreover, the ignition duration was 0.02 s, which gives two sparks generated from an AC transformer with an output voltage of 10 kV and a current of 20 mA. At the top of the channel, four Kistler pressure transducers spaced 250, 450, 650, and 850 mm from the closed end of the channel recorded the explosion pressure. A Photron SA-1 high-speed camera records the flame propagation with frame rates ranging from 10 000 and 22 500 frames per second, depending on the flame propagation speed.

The gas compositions shown in Table 1 are taken from a previously published study by Henriksen et al. (M. Henriksen et al., 2021). The High LBV Li-ion gas composition has a relatively high LBV compared to other published Li-ion vent gas compositions (Baird et al., 2020; M. Henriksen et al., 2021), and the Simplified Li-ion gas composition is a pseudo/simplified Li-ion vent gas, which has an LBV in the same range as several different types of LIBs (M. Henriksen et al., 2021). The High LBV Li-ion gas was supplied from a premixed gas bottle prepared by a supplier, whereas two separate gas bottles supplied the hydrogen and methane for the Simplified Li-ion gas. Furthermore, the φ and the fuel ratio in the Simplified Li-ion gas were controlled by adjusting separate rotameters for the fuel and air. All the gas bottles had a purity above 99.95%.

The flame front position and velocity were determined using an in-house developed image processing code from the high-speed video. The pressure data, flame front position, and velocity were post-processed by a Savitzky-Golay filter (Savitzky and Golay, 1964) before further analysis.

2.2. CFD simulation

The XiFoam model/solver, part of the OpenFOAM toolbox's (CFD Direct, 2021; H. G. Weller et al., 1998) official release, was used for all simulations. In XiFoam, the flame is modeled as a laminar flamelet, which assumes that the turbulent premixed flame comprises a group of laminar flamelets (Peters, 1988). With the laminar flamelet approach, a regress variable (b) can express the flame propagation. Eq. (1) shows the transport equation for regress variable b implemented in the XiFoam model.

$$\frac{\partial}{\partial t}(\rho b) + \nabla.(\rho \boldsymbol{U} b) + \nabla.(\rho D \nabla b) = -\rho_u S_u \Xi |\nabla b| \tag{1}$$

where: b – reaction regress variable [-], ρ – density [kg/m^3], $\boldsymbol{U}$ – velocity vector [m/s], D – diffusion coefficient [m^2/s], S_u – laminar burning velocity (LBV) [m/s], Ξ – turbulent and laminar flame speed ratio [-].

The LBV (S_u) in the source term in Eq. (1) is calculated from the Gülder equation (Gülder, 1984). Ξ models the contribution which the subgrid turbulence has on the flame speed. Eq. (2) shows the transport equation for Ξ. Additional information about the XiFoam combustion model can be found in the original publications by Weller et al. (H.G. Weller et al., 1998; Weller et al., 1991).

$$\frac{\partial \Xi}{\partial t} + \widehat{U}_s \cdot \nabla \Xi = G\Xi - R(\Xi - 1) + (\sigma_s - \sigma_t)\Xi \tag{2}$$

where: Ξ is the subgrid wrinkling factor; U_s is the surface filter velocity; G is the turbulence generation rate; R is the turbulence removal rate; σ_s is the surface-filtered strain rate; σ_t is the resolved strain rate.

To determine the discretized schemes and model parameters to apply for all simulations, we simulated the High LBV Li-ion gas at φ equal to

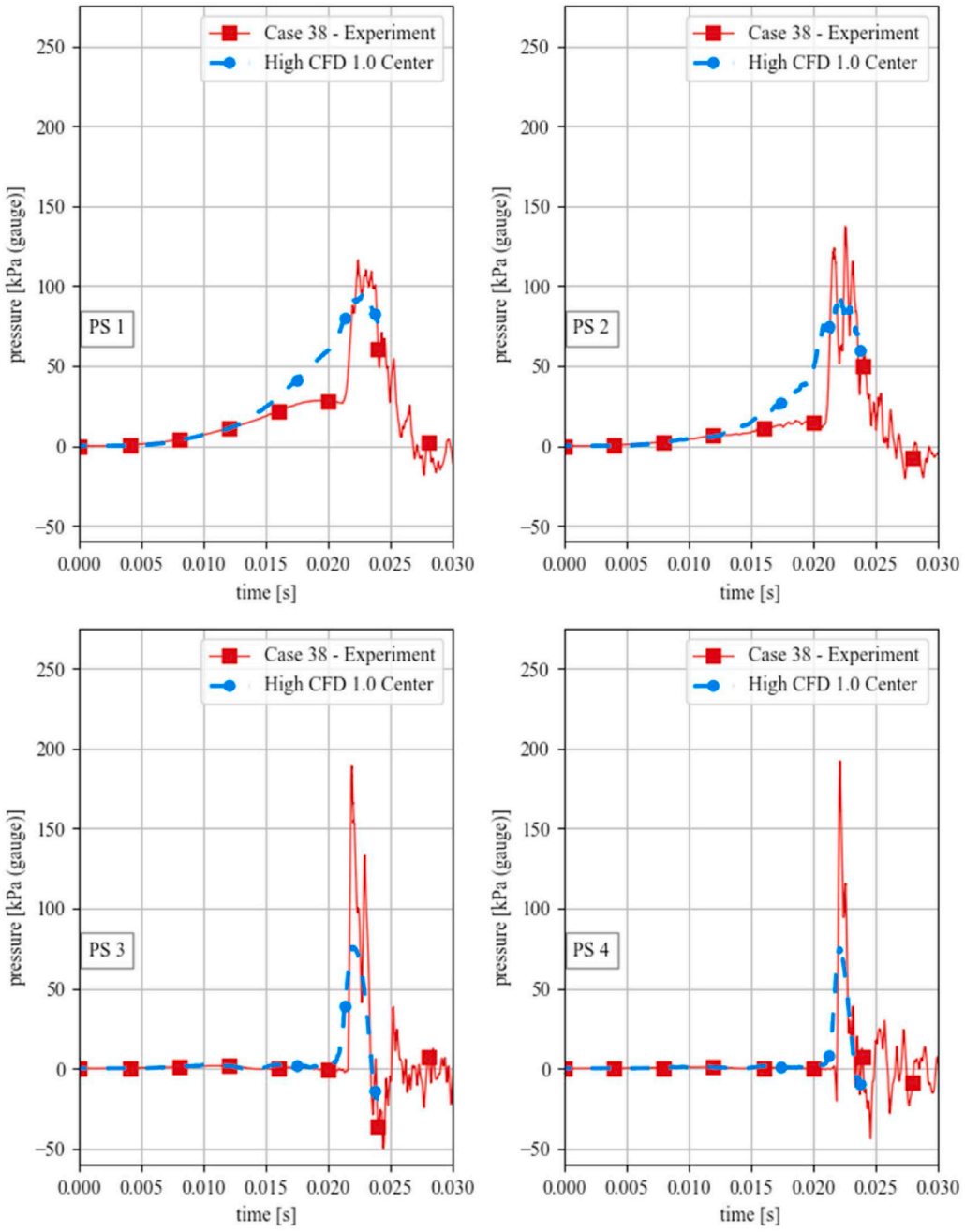

Fig. 3. Comparison of the temporal evolution of the pressure for the four pressure sensors (PS1, PS2, PS3, and PS4) for Case 38 and the simulated case High CFD 1.0 center.

1.0 with the center channel geometry and compared the results to an experiment with similar conditions (case 38). For the comparison, the focus was on the flame propagation and explosion pressure in pressure sensor 1 (PS1). This comparison led to the following discretized schemes and models presented.

The time integration was discretized using the second-order Crank-Nicolson scheme with a ratio of 0.6 forward Euler and 0.4 Crank-Nicolson. For the gradient and Laplacian/diffusion terms, the second-order linear scheme was used. Furthermore, the three different second-order schemes, linear, linear-upwind, and limited-linear, were used for the divergence schemes. The discretized equations are solved using the PIMPLE algorithm, a combination of PISO (Pressure Implicit with Splitting Operators) and SIMPLE (Semi-Implicit Method for Pressure-Linked Equations).

Large-eddy simulation (LES) was chosen as the turbulence approach, using the subgrid model proposed by Akira Yoshizawa (1986) for compressible turbulent shear flows. The Van-Driest dampening function was used for wall turbulence treatment, with the A^+ coefficient and ΔC equal 26 and 0.158, respectively.

The combustion, transport, and thermodynamic properties were generated using the *mech2Foam* code (Henriksen and Bjerketvedt, 2021a, p. 2). *mech2Foam* generates the NASA polynomial (McBride et al., 1993), Sutherland (1893), and Gülder coefficients using a specified reaction mechanism. A study by Henriksen et al. (M. Henriksen et al., 2021) has demonstrated that the GRI-Mech 3.0 reaction mechanism accurately predicts the LBV for the two gas compositions in Table 1, and therefore use in this study.

Two computer-aided design (CAD) geometries were drawn, with the exact dimensions as the experimental channel geometries. The initial cell size is set by the background mesh generated in the utility blochMesh, with the initial cell size in the channel of 4 mm in all directions. At the open end of the channel, the cell size expands linearly in all directions to 8 mm, creating a rectangular frustum with a length of 500 mm outside the rectangular channel, as illustrated in Fig. 2 a). Using the snappyHexMesh utility in OpenFOAM, the background mesh is snapped to the CAD drawing and refined to three layers with half the initial cell size at the channel walls. At the cylinder/cell walls, the first three layers have a fourth of the initial cell size, followed by an additional three

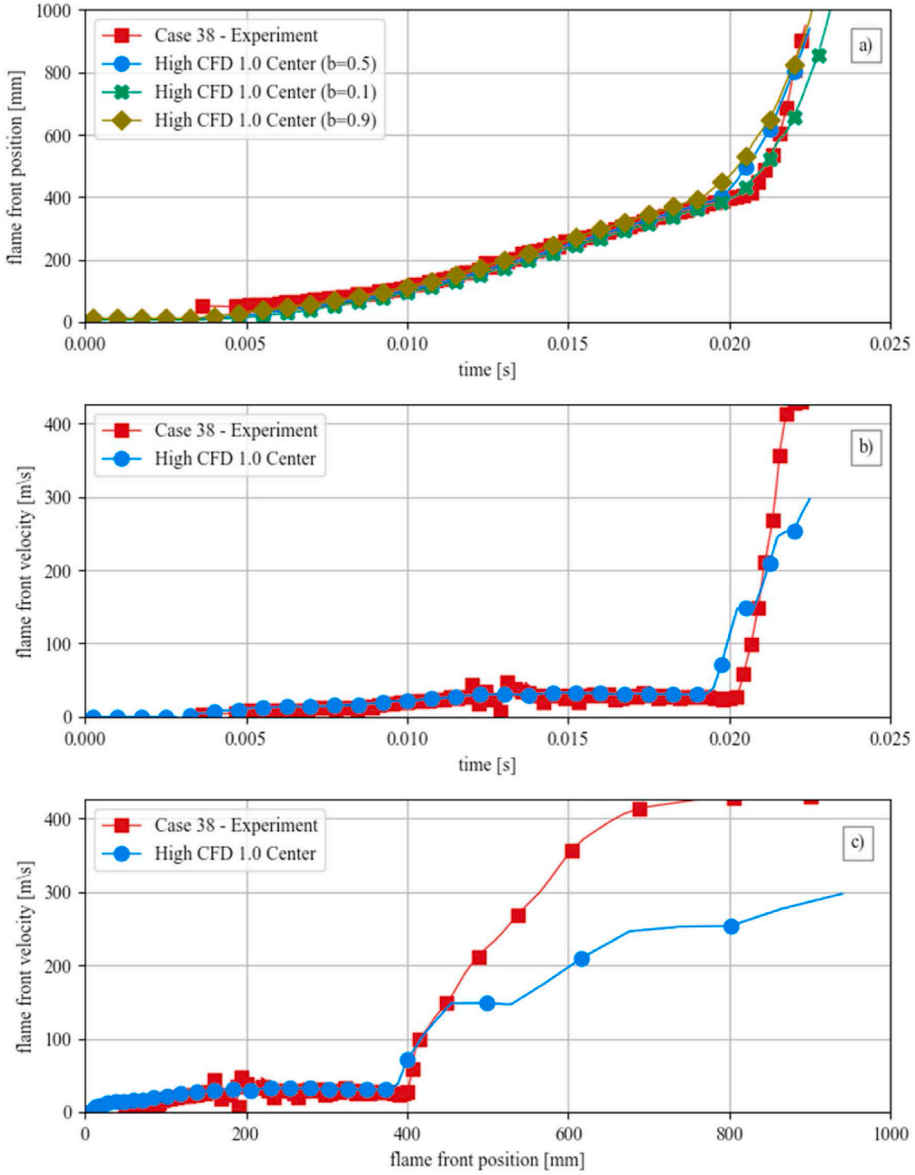

Fig. 4. Comparison of experimental Case 38 and the simulation case High CFD 1.0 center. a): Comparison of the temporal evolution of the flame front position; b): Comparison of the temporal evolution of the flame front velocity; c): Comparison of the spatial evolution of the flame front velocity.

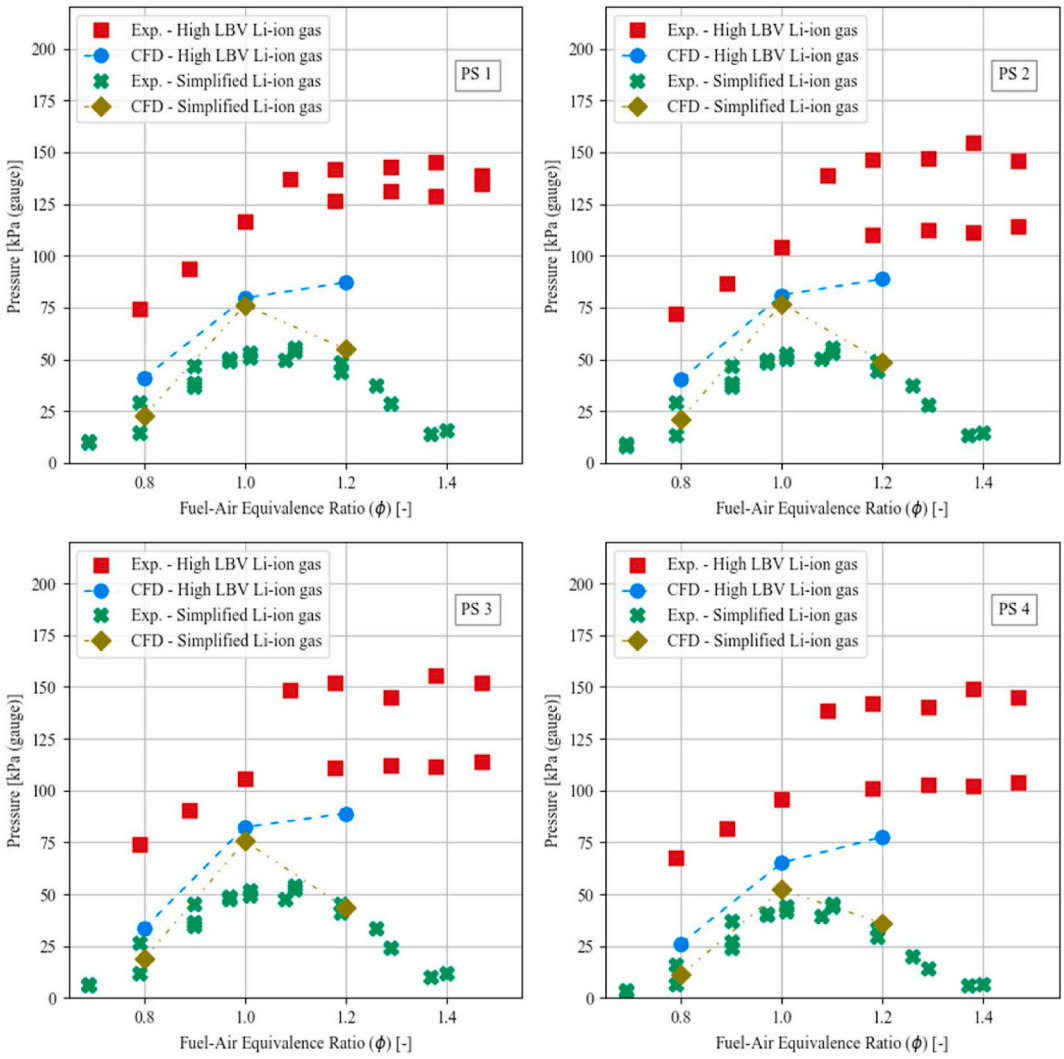

Fig. 5. The maximum pressure peak for each pressure sensor for the inner channel geometry High LBV Li-ion gas and the Simplified Li-ion gas experiments and numerical simulations.

layers with half the initial cell size, as shown in Fig. 2 c). The total amount of cells for the inner and center channel geometry was 944 849 and 945 843, respectively.

Fig. 2 a) shows that the boundaries are divided into two domains, wall boundaries and open boundaries. Typical wall boundary conditions (grey part of Fig. 2 a)) were set on the channel walls, and typical open boundary conditions (black part of Fig. 2 a)) were set on the boundaries outside the channel. A volume outside the channel was included in the computational domain to reduce errors caused by the outlet boundary conditions. Inside the channel, the species were premixed fuel and air, and outside of the channel, there was only air. The atmospheric conditions for the simulations were 293 K and 101.3 kPa (absolute), similar to the overall experimental conditions. Table 2 lists all the wall and open boundary conditions used for each variable in the simulations.

Finally, we referred to the OpenFOAM user guide to further explain the boundary conditions and discretization schemes (CFD Direct, 2021). The CFD base case is given in the supplementary materials.

In Table 3, all the experimental cases are listed, with gas composition, φ, channel geometry, and the corresponding CFD simulation case name.

3. Results

The model parameters and discretization schemes used for all simulations were determined by comparing the experimental Case 38 and the High CFD 1.0 center simulation case. Fig. 3 compares the recorded pressure from the four pressure sensors (PS) for these two cases. The simulated explosion pressure at PS1 was used as one of the target parameters in the optimization, and therefore has the lowest deviation of the four pressure sensors. PS4 had the highest difference in the maximum pressure peak of 117 kPa and a relative deviation of 61%.

Fig. 4 shows the comparison of Case 38 and the simulation case High CFD 1.0 center for the temporal flame front position and flame front velocity and the spatial flame front velocity. The flame front position in Fig. 4 a) shows a good agreement between the simulated and experimental results. Fig. 4b) and c) shows that the simulated flame acceleration is under-predicted after the flame reaches the cylinders.

Fig. 5 shows the numerical and experimental maximum pressure peaks for each pressure sensor recorded in the inner channel geometry for the High LBV Li-ion gas and the Simplified Li-ion gas. The highest maximum pressure for the High LBV Li-ion gas was 156 kPa (gauge), recorded at PS3 in case 10 ($\varphi = 1.38$). In the numerical simulations, the highest maximum pressure of 89 kPa (gauge) was in the High CFD 1.2

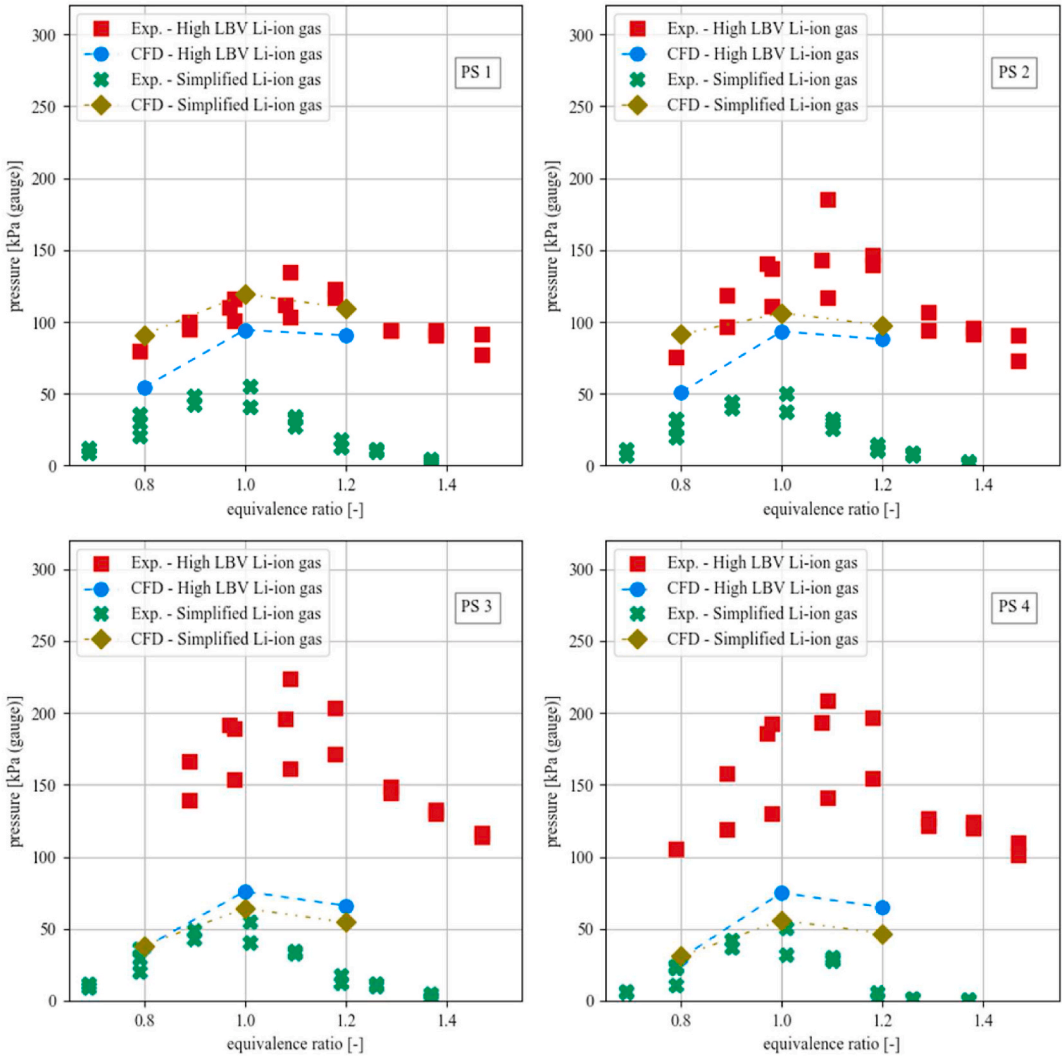

Fig. 6. The maximum pressure peak for each pressure sensor for the center channel geometry High LBV Li-ion gas and the Simplified Li-ion gas experiments and numerical simulations.

Inner case. Furthermore, the average absolute deviation between the experimental and simulated maximum pressures for the High LBV Li-ion gas is 38 kPa, with a maximum absolute deviation of 64 kPa for case 05 (at PS4).

For the Simplified Li-ion gas experiments, the highest maximum pressure peak was 56 kPa (gauge) (at PS1) in case 26 ($\varphi = 1.10$). The highest simulated maximum pressure was 77 kPa (gauge) (at PS2) in the Simple CFD 1.0 Inner case. Finally, the average absolute deviation between the experiments and simulations for the Simplified Li-ion gas was 14 kPa, with a maximum deviation of 28 kPa for case 21 (at PS2).

Fig. 6 shows the simulated and experimental maximum pressure peaks from the center channel geometry for each pressure sensor. For the High LBV Li-ion gas, the highest experimental maximum pressure of 223 kPa (gauge) was measured at PS3 for case 41 ($\varphi = 1.09$), and the highest simulated maximum pressure of 94 kPa (gauge) was measured at PS1 for the High CFD 1.2 Center case. Moreover, the average absolute deviance between the experimental and numerical results was 64 kPa, with a maximum absolute deviation of 137 kPa for case 43 (at PS3).

The highest maximum pressure peaks for the Simplified Li-ion gas were 55 kPa (gauge) measured at PS1 in case 58 ($\varphi = 1.01$) and 119 kPa (gauge) at PS1 in simulation case Simple CFD 1.0 Center. The average absolute deviation was 50 kPa, and the maximum absolute deviation was 97 kPa PS1 for case 62.

Fig. 7 shows the positive impulses for each pressure sensor for the inner channel geometry experiments and simulations. The positive impulse was calculated by numerically integrating the maximum pressure peak, with the upper and lower integral limits set to one-tenth of the maximum pressure. All maximum values for the experimental and simulated positive impulses were recorded on the first pressure sensor (PS1) for both gas compositions.

The maximum experimental positive impulse was 188 kPa ms and 160 kPa ms for the High LBV Li-ion gas (case 11, $\varphi = 1.47$) and the Simplified Li-ion gas (case 26, $\varphi = 1.10$) in the inner channel geometry, respectively. In the simulations, the maximum positive impulse was 313 kPa ms (High CFD 1.2 Inner) and 280 kPa ms (Simple CFD 1.0 Inner) for the High LBV Li-ion gas and the Simplified Li-ion gas, respectively. The absolute average deviation between simulation and experimental positive impulse results for the High LBV Li-ion gas was 100 kPa ms, whereas 82 kPa ms for the Simplified Li-ion gas. Furthermore, the maximum absolute deviation was 171 kPa ms (case 06, at PS2) and 144 kPa ms

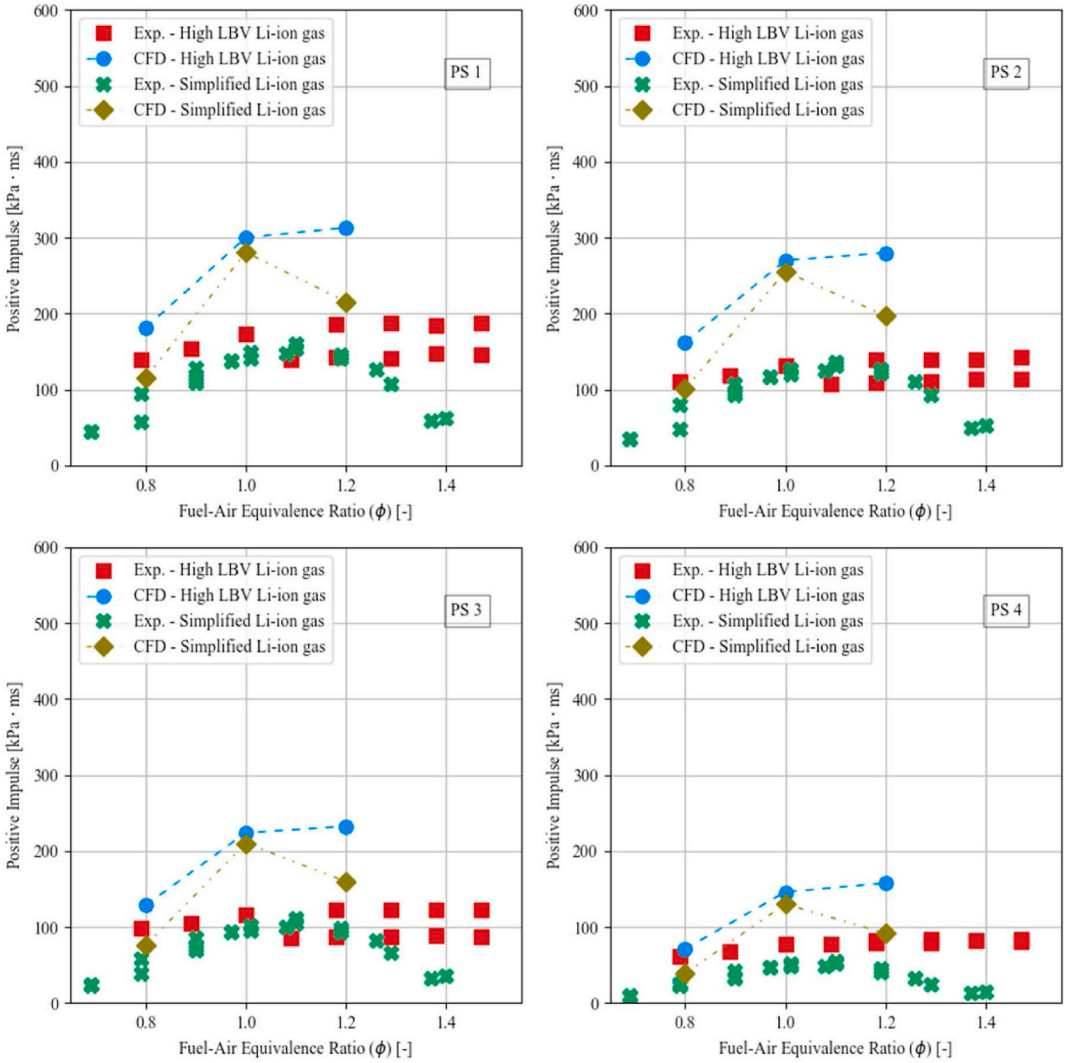

Fig. 7. The positive impulse for each pressure sensor for the inner channel geometry High LBV Li-ion gas and the Simplified Li-ion gas experiments and numerical simulations.

(case 20, at PS1) for the High LBV Li-ion gas and Simplified Li-ion gas, respectively.

Fig. 8 shows the experimental and numerically positive impulses for each pressure sensor for all center channel geometry cases. All maximum positive impulses were recorded on the first pressure sensor (PS1) for both gas compositions in the experiments and numerical simulations, like the inner channel geometry cases. For the High LBV Li-ion gas, the experimental maximum positive impulse was 591 kPa ms (case 42, $\varphi = 1.18$), whereas in the simulation, 666 kPa ms for case High CFD 1.2 Center. The absolute average deviation between the simulation and experiments for the High LBV Li-ion gas was 100 kPa ms, with a maximum absolute deviation of 243 kPa ms for case 36 (at PS2).

For the Simplified Li-ion gas, the experimental maximum positive impulse was 324 kPa ms (case 58, $\varphi = 1.01$). In the simulation, the maximum positive impulse was 743 kPa ms measured in the Simple CFD 1.0 Center case. Moreover, the absolute average deviation between the experimental and numerical positive impulse is 206 kPa ms, with a maximum absolute deviation of 532 kPa ms in case 62 (at PS1).

Further quantification of the model performance was done by calculating the statistical quantities, mean geometric variance (VG), and mean geometric bias (MG) for the temporal pressure evolution, maximum pressure, positive impulse, and spatial evolution of the flame front velocity. Table 4 presents the criteria used to assess the model performance, taken from the model evaluation protocol for the HySEA project (Hisken et al., 2020), which is based upon the MEGGE protocol (Model Evaluation Group Gas Explosion, 1996).

Fig. 9 shows the MG and VG values for the inner channel geometry High LBV Li-ion gas and Simplified Li-ion gas cases. The calculated VG and MG values for the temporal pressure evolution are within the limit for excellent model performance, as shown in Fig. 9 a). For the MG and VG values in Fig. 9 b) (maximum pressure peak), only case 42 had an MG value slightly above the limit for excellent model performance. The MG and VG values shown in Fig. 9a) and b) indicate that the XiFoam model predicted the maximum pressure peaks and temporal pressure evolution accurately for both gas compositions in the inner channel geometry. For several cases, the MG values for the positive impulse were outside the acceptable limit. The spatial flame front velocity MG and VG values were within the acceptable limits for all, except case 15.

The overall XiFoam model performance was evaluated by equally weighting the arithmetic mean MG and VG values of the temporal pressure evolution, maximum pressure peaks, positive impulse, and spatial evolution of the flame front velocity. For the inner channel geometry, the overall average MG and VG were 0.96 and 1.26 for the High LBV Li-ion gas, respectively, whereas the overall average MG and VG for the Simplified Li-ion gas were 0.89 and 1.36, respectively. Both the overall averaged MG and VG for the two gas compositions are within the acceptable performance criteria.

Fig. 10 shows the MG and VG values for the center channel geometry

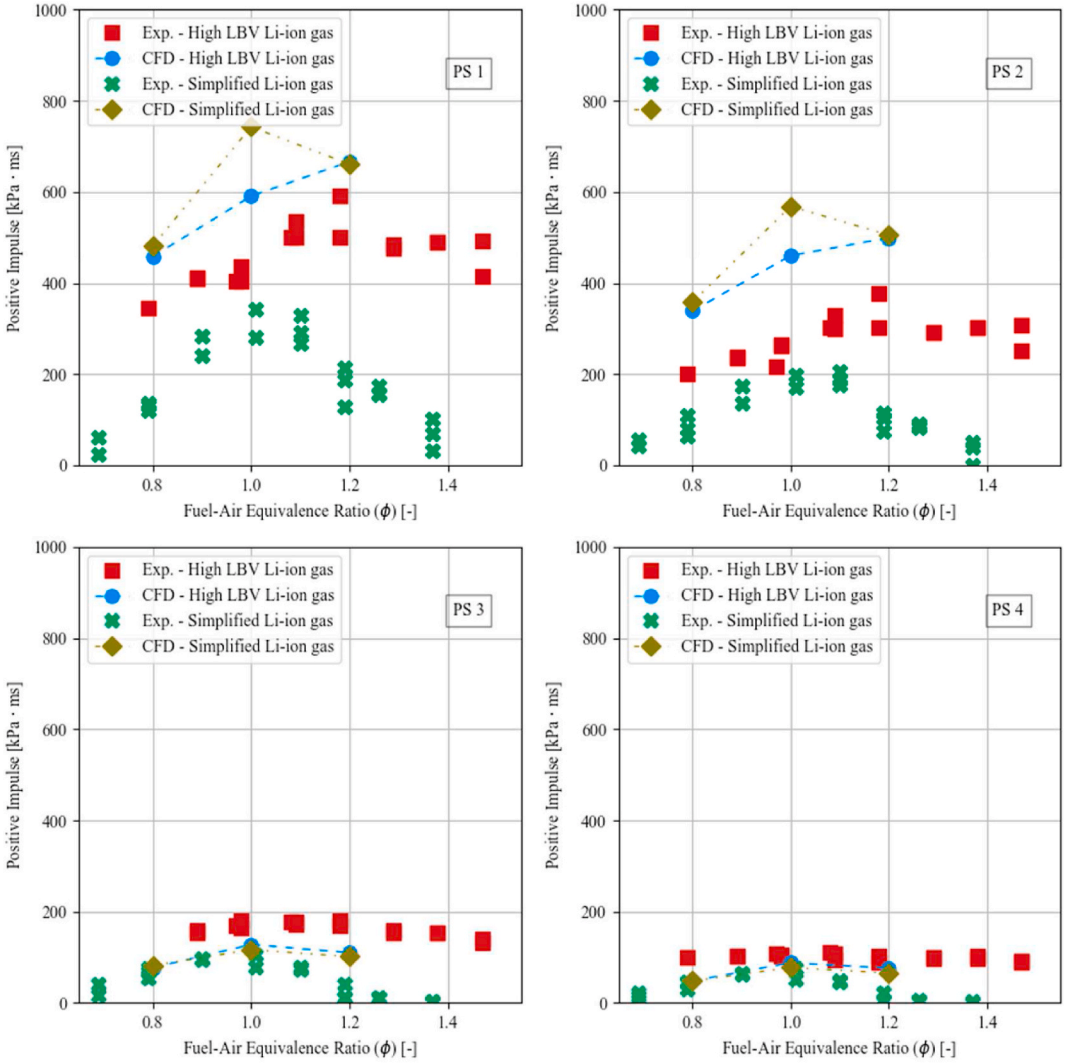

Fig. 8. The positive impulse for each pressure sensor for the center channel geometry High LBV Li-ion gas and the Simplified Li-ion gas experiments and numerical simulations.

Table 4
Criteria for evaluating model performance for a specific variable from the model evaluation protocol for the HySEA project (Hisken et al., 2020).

The scale of model performance	MG and VG limits	
Excellent	$0.7 < MG < 1.3$	[Solid vertical lines]
	$VG < 1.6$	[Solid horizontal line]
Acceptable	$0.5 < MG < 2.0$	[Dashed vertical lines]
	$VG < 3.3$	[Dashed horizontal line]
Poor	$0.5 > MG > 2.0$	
	$VG > 3.3$	

cases. The MG and VG values for the temporal pressure evolution and the maximum pressure are all within the acceptable criteria for both gas compositions. The positive impulse MG and VG values for the High LBV Li-ion cases are all within the excellent performance criterion. However, for the Simplified Li-ion gas, only case 57 is within the MG acceptable criterion. This poor model performance is reflected in the predicted positive impulse of the Simplified Li-ion gas in Fig. 8. For all cases, the spatial evolution of the flame front velocity MG and VG values are within the acceptable criteria for both gas compositions, with seven out of ten within the excellent criteria.

The overall averaged MG and VG values were 1.10 and 1.14 for the High LBV Li-ion gas, respectively. For the Simplified Li-ion gas, the overall average MG and VG values were 0.80 1.86, respectively. Furthermore, the overall average MG and VG values were within the excellent performance criteria for the High LBV Li-ion gas. For the Simplified Li-ion gas, the overall average MG and VG were within acceptable model performance criteria.

For the unfiltered experimental results, we refer to the dataset *Experiments of Premixed Gas Explosion in a 1-m Channel Partly Filled with 18650 Cell Geometry* (Henriksen and Bjerketvedt (2021b)).

4. Discussion

4.1. Variance in the experimental results

Figs. 5 and 6 shows that parallel experiments can give significantly different maximum pressures peaks. These differences in the results are especially noticeable for the center channel geometry High LBV Li-ion gas experiments at pressure sensors 2, 3, and 4. The differences in the maximum pressure peaks can be as high as 60–70 kPa, which is in the same range as the more significant deviations between the simulation and experimental results. Although minor differences were noticed in the flame front velocity and surface in parallel experiments, no phenomena or measured parameter could be attributed to the experiments with an increased or reduced maximum pressure peak. It is common to compare simulated and experimental maximum pressure peaks results

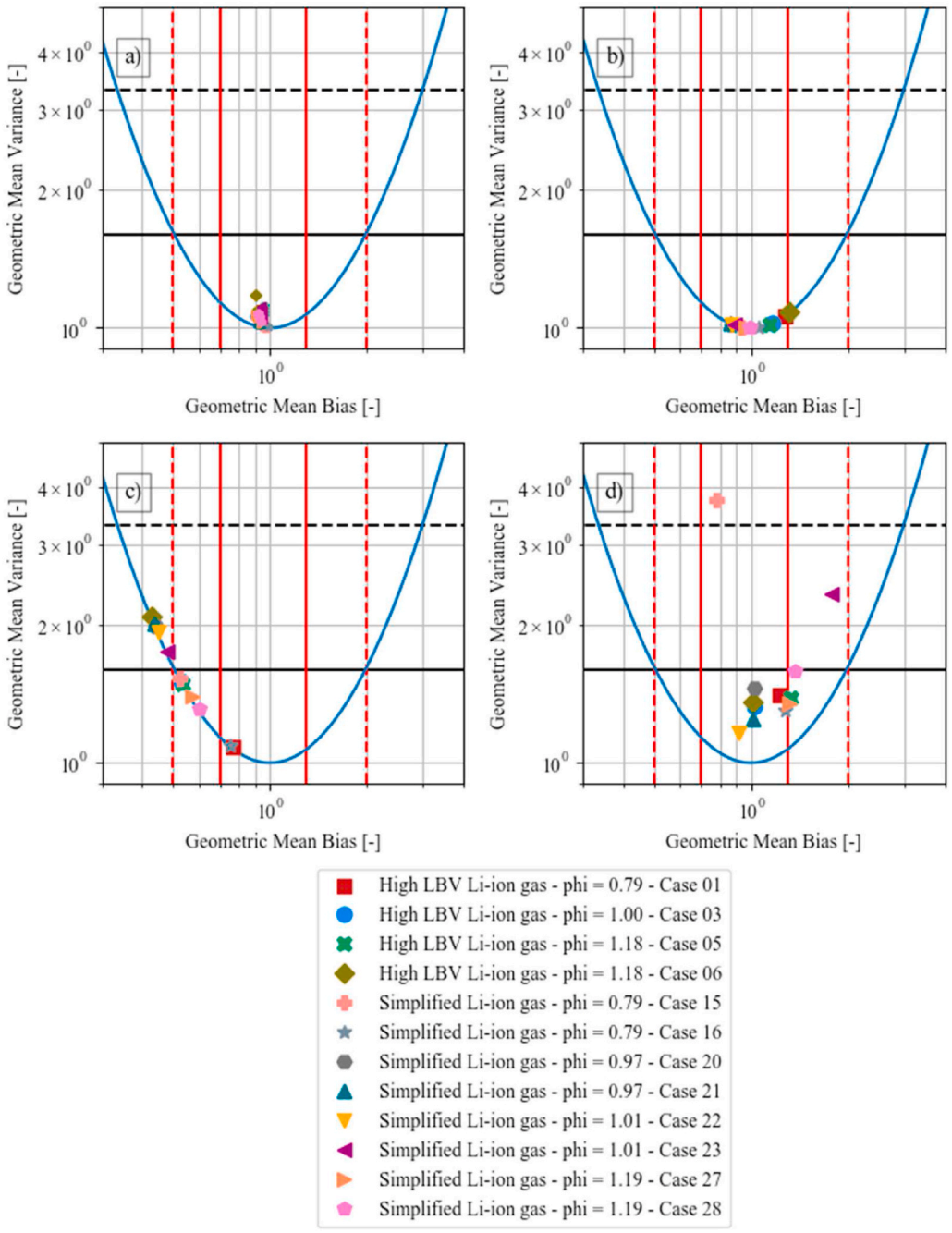

Fig. 9. The mean geometric bias and the mean geometric variance for the High LBV Li-ion gas and the Simplified Li-ion gas in the inner channel geometry; a) Temporal pressure evolution; b) Maximum pressure; c) Positive impulse; d) Spatial evolution of the flame front velocity.

(Diakow et al., 2018; Shen et al., 2020); however, it may not be an ideal comparable parameter due to potential variance between parallel experiments as observed in this study.

4.2. Model performance

Based on the overall average MG and VG values, the XiFoam model performed acceptable for the Simplified Li-ion gas and performed excellently for the High LBV Li-ion gas for both channel geometries. XiFoam had the highest model performance for the High LBV Li-ion gas in the center channel geometry, which is expected since the model parameters were adjusted to this configuration at a φ equal to 1.0. However, the model showed discrepancies in predict the maximum pressure peaks recorded at PS3 and PS4, as seen in Fig. 6. In the simulations, the flame thickness grows as it propagates through the geometry. This increase in flame thickness probably dampens the maximum pressure peaks caused by the rapid increase in flame acceleration when the flame passes through the cylinders. Although the model does not predict the maximum pressure peaks at these sensors, the positive impulse is predicated with less deviation.

The XiFoam model performance for the Simplified Li-ion gas was lower than for the High LBV Li-ion gas, based on the MG and VG values. Although the overall average model performance for the center channel geometry Simplified Li-ion gas cases were within the acceptable criteria, only one case was within acceptable performance criteria for positive impulse, as seen in Fig. 10 c). Additionally, there is a significant discrepancy between the simulated and experimental flame front position before the flame reaches the cylinders for these cases. This

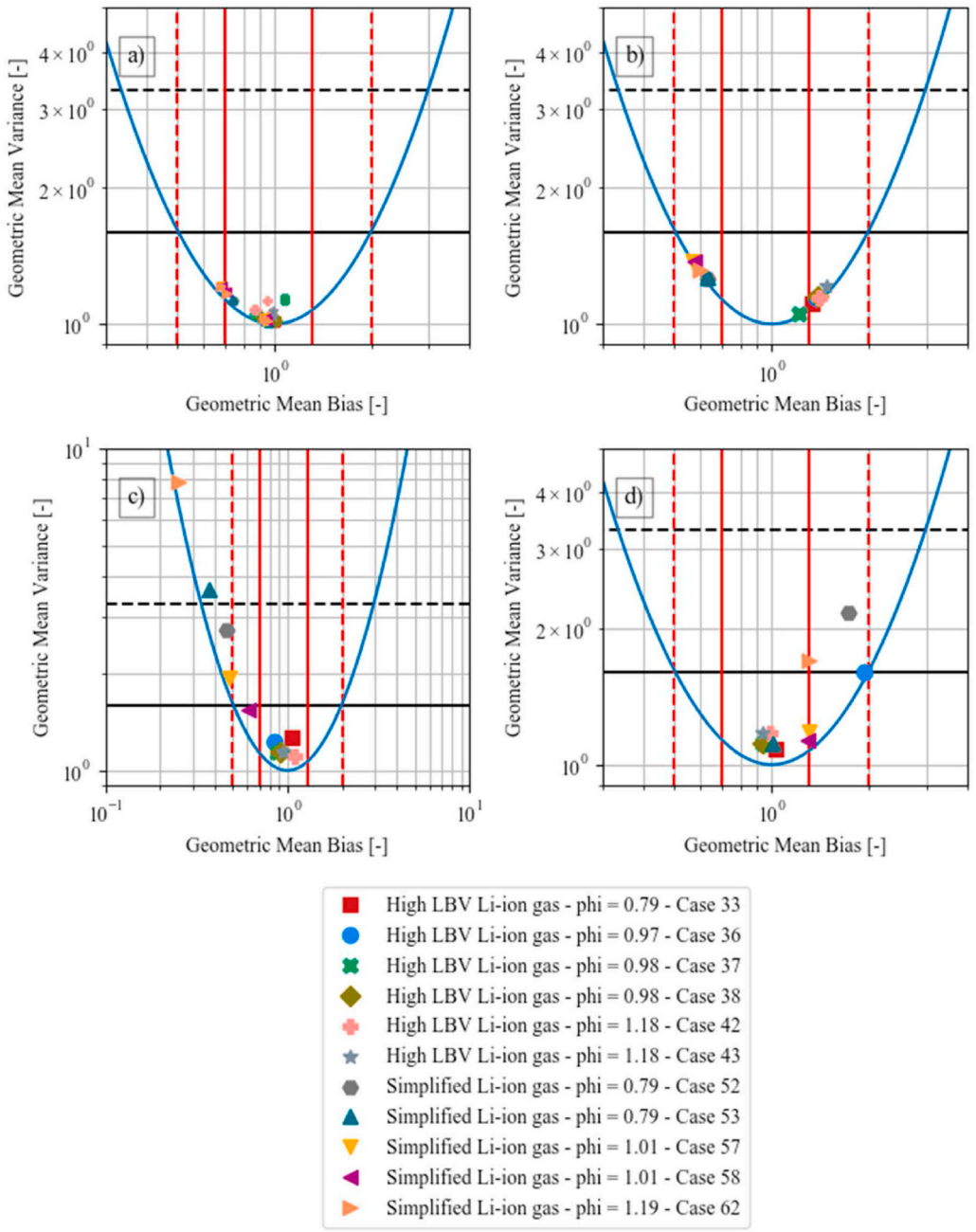

Fig. 10. The mean geometric bias and the mean geometric variance for the High LBV Li-ion gas and the Simplified Li-ion gas in the center channel geometry; a) Temporal pressure evolution; b) Maximum pressure; c) Positive impulse; d) Spatial evolution of the flame front velocity.

discrepancy reveals that the flame accelerates more rapidly in the initial stages in the simulation compared to the experiments. The higher flame acceleration leads to the higher maximum pressure peaks, as seen in Fig. 6a) and b) for the Simplified Li-ion gas. Conversely, the experimental and simulated flame acceleration is in the same range for the inner channel geometry Simplified Li-ion gas cases, resulting in better model performance.

4.3. Model parameters and discretization

There are many different model parameters and discretization schemes to adjust and choose from in the OpenFOAM toolbox. Our focus was on the XiFoam combustion parameters and the discretization of time and divergence terms to limit the number of parameters and settings. However, other model parameters or discretization schemes could also significantly impact the simulation performance than those chosen in this study.

The Xi (Ξ) variable in Eq. (1) and Eq. (2) is the ratio between laminar and turbulent burning velocity. Xi, cannot be lower than one and will thus only increase or not affect the propagation velocity. For the center channel geometry, the initial flame acceleration was slightly higher in most simulation cases compared to the experiments. This discrepancy in flame acceleration was especially noticeable for the Simplified Li-ion gas cases. In the combustion property file, three variables can be adjusted to affect the value of Xi, *XiCoef*, *XiShapeCoef*, and *uPrimeCoef*. Using the Xi transport model, only changes to the *uPrimeCoef* significantly altered flame acceleration. *uPrimeCoef* is multiplied with the turbulent kinetic energy (k) used to evaluate the Xi value. Initially, the *uPrimeCoef* coefficient was set to 0.6, which has given good results in previous simulations and fitted reasonably well for the High CFD 1.0 Center validation

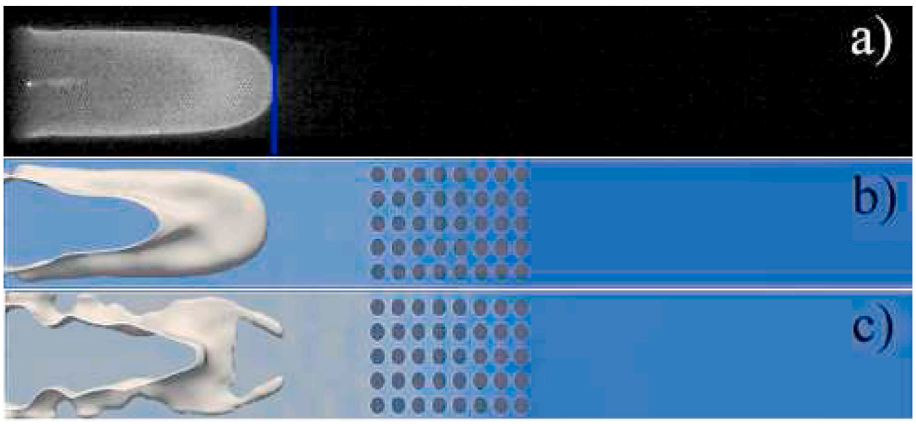

Fig. 11. Examples of images of the experimental and simulated flame propagation in the center channel geometry. a): Image from the high-speed video; b): Typical numerical flame surface (isosurface of the regress variable b at 0.5); c) Odd-shaped flame surface due to changes in the numerical schemes or combustion parameters (isosurface regress variable b at 0.5).

case. However, for the center channel geometry Simplified Li-ion gas simulation cases, a lower value of the *uPrimeCoef* coefficient would have reduced flame acceleration and thus lower maximum pressure peaks. For example, altering the *uPrimeCoef* coefficient to 0.1 in the Simple CFD 1.0 Center simulation case will result in a maximum pressure peak of 25 kPa (gauge). Changes to *uPrimeCoef* could lead to an odd-shaped flame surface compared to experiments and previous simulations, as depicted in Fig. 11 c). The odd-shaped flame surface can cause significant changes to the predicted flame front position and velocity.

Different discretization schemes were tested to analyze if they had any significant effect on the solution. Discretizing time using first-order forward Euler resulted in numerically stable simulations, with little to no effect when changing the discretization schemes for the divergence terms. However, changing the time discretization scheme to second-order backward Euler or Crank-Nicolson significantly impacted the flame propagation. Using the second-order backward scheme would lead to convergence errors. Using the Crank-Nicolson scheme, the intended simulation time was achieved (for most cases) with a Crank-Nicolson coefficient between 0.1 and 0.6. The larger Crank-Nicolson coefficient usually increased the flame acceleration and thus the maximum pressure peak. For example, by increasing the coefficient to 0.6 for the High CFD 1.0 Center simulation case, the maximum pressure peak was 450 kPa (gauge), 300 kPa higher than for the simulation case using a coefficient of 0.4. Although a higher coefficient increased the flame acceleration, it could also lead to similar odd-shaped flames, as shown in Fig. 11 c). Numerical instabilities probably cause the odd-shaped flame surfaces. Thus, a linearUpwind discretization scheme was used to minimize the numerical instability and retain second-order accuracy for most divergence terms.

Adjusting the value of *uPrimeCoef* and the Crank-Nicolson coefficient in post-analysis for each simulation case, it is possible to predict the desired target parameter fairly accurately, whether it be flame acceleration or maximum pressure peak, or positive impulse. However, accurately predicting all three of these parameters in the same simulation with the XiFoam model is proven to be challenging.

Finally, one of the reasons that the XiFoam was chosen as the combustion model was its capability to simulate both small-scale (Mathias Henriksen et al., 2021) and large-scale (Li et al., 2021) cases/geometries. Although the XiFoam model gives an overall acceptable model performance for the two geometries and gas mixtures, it is uncertain how well XiFoam will perform for large-scale Li-ion battery incidents. Validating CFD combustion models with small/laboratory-scale experiments is not uncommon (Elshimy et al., 2021; Hansen et al., 2005; Middha et al., 2007; Oran and Gamezo, 2007); however, it does not remove the necessity of large-scale experiment comparison. As of now, there are few large-scale experiments relevant for Li-ion battery incidents CFD comparison. The comparison in this study is a step forward, showing the capability of predicting small-scale Li-ion battery explosions and addressing some of the challenges encountered using the XiFoam combustion model. To improve the XiFoam model confidence further, the focus should be on large-scale experiments of battery incidents in future research.

4.4. Final observations

In the simulations, the pressure peaks are broader than in most experiments, making it impossible to predict both the maximum pressure peak and the positive impulse with extreme precision. In the simulations, the flame thickness is initially thin with the thickness of a few cells, but as it propagates, it broadens and can grow to a thickness larger than 200 mm. However, the flame thickness of an actual flame is at least a hundred times thinner than this. Since the numerical flame thickness is large, the total heat of combustion is released over a larger volume than the actual experimental flame, and thus generating a broader pressure peak. A possible solution for this issue in the XiFoam model could be to reduce the cell size; unfortunately, this could not be investigated further due to limited computational resources.

For the experimental center channel geometry Simplified Li-ion gas cases, only the cases with a φ below 1.19 (case 50 to 61) would propagate through the cylinders without quenching. Most cases would completely quench within the cylinders in the experiments with φ 1.19 and above (case 62 to 70). However, a few experiments (case 63, 67, 68, and 69) eventually propagated through, although the time from no visible flame to visible flame in the high-speed video was on average 0.21 s. By contrast, the average time for the flame to reach the cylinders after ignition for these cases was 0.05 s. A common occurrence for cases 63, 67, 68, and 69, the first visible flame after "quenching," was always in the top part of the channel.

Case 62, which had a φ of 1.19, propagated past the cylinders similar to those experimental cases with a φ below 1.19. For case 62, the flame was partly quenched while propagated in the center of the cylinders. However, the flame continued to propagate without quenching in the top and bottom of the channel. Since case 62 propagated through the cylinders, similarly to the experiments with φ below 1.19, it was the only experimental case compared to the Simple CFD 1.2 Center simulation case.

Conversely, all the center channel geometry High LBV Li-ion gas cases propagated through without any indication of quenching. The LBV for the High LBV Li-ion gas is more than twice that of the Simplified Li-ion gas at similar φ (M. Henriksen et al., 2021), which is an essential parameter for this phenomenon. The quenching may be caused by a highly turbulent flow, which may be violating the XiFoam laminar

flamelet assumption. Further investigation is needed to explain this phenomenon more deeply, which is beyond the scope of this study.

5. Conclusion

This study examined the XiFoam model performance, a combustion solver part of the open-source CFD toolbox OpenFOAM. The XiFoam model performance was evaluated by comparing numerical simulations and experiments of premixed gas explosions in a 1-m explosion channel partly filled with 18650 cell-like cylinders. In addition to comparing two geometries with different locations of the 40 18650 cell-like cylinders, two gas compositions with significantly different LBV at several φ were compared. The model performance was based on the prediction accuracy of the temporal pressure evolution, maximum pressure peak, positive impulse, and spatial evolution of the flame front velocity.

Based upon the overall average MG and VG values and the model performance criteria in Table 4, the XiFoam had an overall acceptable model performance. XiFoam had the highest prediction accuracy for the center channel geometry High LBV Li-ion gas cases; however, this was expected since one of these cases was used to determine the combustion model parameters and discretization schemes. XiFoam had the lowest prediction accuracy for the center channel geometry Simplified Li-ion gas cases. The lower prediction accuracy was mainly due to an over-predicted flame acceleration in the initial laminar flame propagation stage.

Adjusting the combustion parameter *uPrimeCoef* and the Crank-Nicolson coefficient for the time discretization would significantly change the flame propagation and thus the simulation results. By adjusting these parameters in post-analysis for each simulation, one can increase the prediction accuracy significantly. However, predicting with high precision the maximum pressure peak and positive impulse in the same simulation is difficult with the XiFoam combustion model.

Although the XiFoam overall prediction accuracy for the two gas mixtures with the channel geometries was within the acceptable model performance criteria, it is uncertain the XiFoam model would perform for large-scale and more realistic geometry, like a BESS. In future research, the XiFoam model should be compared with large-scale experiments of battery incidents to improve on the XiFoam model assessment done in this study.

Credit author statement

Mathias Henriksen: Conceptualization, Methodology, Formal analysis, Writing – original draft, Writing – review & editing. Knut Vaagsaether: Conceptualization, Methodology, Formal analysis, Writing – review & editing, Supervision, Funding acquisition. Joachim Lundberg: Conceptualization, Methodology, Formal analysis, Writing – review & editing, Supervision, Funding acquisition. Sissel Forseth: Formal analysis, Conceptualization, Writing – review & editing, Supervision, Funding acquisition. Dag Bjerketvedt: Conceptualization, Methodology, Formal analysis, Writing – review & editing, Supervision, Funding acquisition.

Declaration of competing interest

The authors declare that they have no known competing financial interests or personal relationships that could have appeared to influence the work reported in this paper.

Acknowledgement

This work was performed within MoZEES, a Norwegian Center for Environment-friendly Energy Research (FME), co-sponsored by the Research Council of Norway (project number 257653) and 40 partners from research, industry and public sector.

Appendix A. Supplementary data

Supplementary data to this article can be found online at https://doi.org/10.1016/j.jlp.2022.104761.

References

Andy, Colthorpe, 2020. Fire at 20MW UK battery storage plant in Liverpool [WWW Document]. Energy Storage News. URL. https://www.energy-storage.news/news/fire-at-20mw-uk-battery-storage-plant-in-liverpool.

Baird, A.R., Archibald, E.J., Marr, K.C., Ezekoye, O.A., 2020. Explosion hazards from lithium-ion battery vent gas. J. Power Sources 446, 227257. https://doi.org/10.1016/j.jpowsour.2019.227257.

Beausoleil, Sophia, 2017. Lithium Batteries Causes Train Car Explosion in NE Houston. KPRC, Click2Houston.

Bjerketvedt, D., Bakke, J.R., Van Wingerden, K., 1997. Gas explosion handbook. J. Hazard Mater. 52, 1–150.

CFD Direct, 2021. OpenFOAM v7 user guide [WWW Document]. OpenFOAM v7 User Guide. URL. https://cfd.direct/openfoam/user-guide-v7/.

CTIF - International Association of Fire and Rescue Services, 2021. Accident Analysis of the Beijing Lithium Battery Explosion Which Killed Two Firefighters [WWW Document]. URL. https://www.ctif.org/news/accident-analysis-beijing-lithium-battery-explosion-which-killed-two-firefighters.

Diakow, P.A., Thomas, J.K., Vivanco, E., 2018. Comparison of large-scale vented deflagration tests to CFD simulations for partially congested enclosures. J. Loss Prev. Process. Ind. 56, 147–154. https://doi.org/10.1016/j.jlp.2018.07.012.

Elshimy, M., Ibrahim, S., Malalasekera, W., 2021. LES – DFSD modelling of vented hydrogen explosions in a small-scale combustion chamber. J. Loss Prev. Process. Ind. 72, 104580. https://doi.org/10.1016/j.jlp.2021.104580.

Fernandes, Y., Bry, A., de Persis, S., 2018. Identification and quantification of gases emitted during abuse tests by overcharge of a commercial Li-ion battery. J. Power Sources 389, 106–119. https://doi.org/10.1016/j.jpowsour.2018.03.034.

Golubkov, A.W., Fuchs, D., Wagner, J., Wiltsche, H., Stangl, C., Fauler, G., Voitic, G., Thaler, A., Hacker, V., 2014. Thermal-runaway experiments on consumer Li-ion batteries with metal-oxide and olivin-type cathodes. RSC Adv. 4, 3633–3642. https://doi.org/10.1039/C3RA45748F.

Golubkov, A.W., Scheikl, S., Planteu, R., Voitic, G., Wiltsche, H., Stangl, C., Fauler, G., Thaler, A., Hacker, V., 2015. Thermal runaway of commercial 18650 Li-ion batteries with LFP and NCA cathodes – impact of state of charge and overcharge. RSC Adv. 5, 57171–57186. https://doi.org/10.1039/C5RA05897J.

Gülder, Ö.L., 1984. Correlations of laminar combustion data for alternative S.I. Engine fuels. In: Presented at the West Coast International Meeting and Exposition. https://doi.org/10.4271/841000.

Hansen, O.R., Middha, P., 2008. CFD-based risk assessment for hydrogen applications. Proc. Safety prog 27, 29–34. https://doi.org/10.1002/prs.10213.

Hansen, O., Renoult, J., Sherman, M., Tieszen, S., 2005. Validation of FLACS-Hydrogen CFD consequence prediction model against large scale H2 explosion experiments in the FLAME facility. In: Presented at the International Conference on Hydrogen Safety.

Hansen, O.R., Hinze, P., Engel, D., Davis, S., 2010. Using computational fluid dynamics (CFD) for blast wave predictions. J. Loss Prev. Process. Ind. 23, 885–906. https://doi.org/10.1016/j.jlp.2010.07.005.

Helgesen, H., 2019. Technical Reference for Li-Ion Battery Explosion Risk and Fire Suppression (Technical No. 2019–1025) (DNV GL, Norway.

Henriksen, M., Bjerketvedt, D., 2021a. mech2Foam - Generating Transport, Combustion, and Thermodynamic Properties for the CFD Solver XiFoam. University of South-Eastern Norway. https://doi.org/10.23642/USN.13721134.V3.

Henriksen, M., Bjerketvedt, D., 2021b. Experiments of Premixed Gas Explosion in a 1-meter Channel Partly Filled with 18650 Cell Geometry. https://doi.org/10.23642/USN.15134442.V1.

Henriksen, M., Vaagsaether, K., Lundberg, J., Forseth, S., Bjerketvedt, D., 2019. Explosion characteristics for Li-ion battery electrolytes at elevated temperatures. J. Hazard Mater. 371, 1–7. https://doi.org/10.1016/j.jhazmat.2019.02.108.

Henriksen, M., Gaathaug, A.V., Vaagsaether, K., Lundberg, J., Forseth, S., Bjerketvedt, D., 2020. Laminar burning velocity of the dimethyl carbonate-air mixture formed by the Li-ion electrolyte solvent. Combust. Explos. Shock Waves 56, 383–393. https://doi.org/10.1134/S0010508220040024.

Henriksen, M., Vaagsaether, K., Lundberg, J., Forseth, S., Bjerketvedt, D., 2021. Laminar burning velocity of gases vented from failed Li-ion batteries. J. Power Sources 506, 230141. https://doi.org/10.1016/j.jpowsour.2021.230141.

Henriksen, Mathias, Vaagsaether, K., Lundberg, J., Forseth, S., Bjerketvedt, D., 2021. Simulation of a premixed explosion of gas vented during Li-ion battery failure. Fire Saf. J. 103478. https://doi.org/10.1016/j.firesaf.2021.103478.

Hill, D., 2020. McMicken Battery Energy Storage System Event Technical Analysis and Recommendations (Technical No. 10209302- HOU- R- 01) (DNV-GL.

Hisken, H., Lakshmipathy, S., Atanga, G., Skjold, T., 2020. Model Evaluation Protocol for HySEA (Gexcon AS.

Johnsplass, J., Henriksen, M., Vaagsaether, K., Lundberg, J., Bjerketvedt, D., 2017. Simulation of Burning Velocities in Gases Vented from Thermal Run-A-Way Lithium Ion Batteries, pp. 157–161. https://doi.org/10.3384/ecp17138157.

Kennedy, R.W., Marr, K.C., Ezekoye, O.A., 2021. Gas release rates and properties from Lithium Cobalt Oxide lithium ion battery arrays. J. Power Sources 487, 229388. https://doi.org/10.1016/j.jpowsour.2020.229388.

Kim, G.-H., Pesaran, A., Spotnitz, R., 2007. A three-dimensional thermal abuse model for lithium-ion cells. J. Power Sources 170, 476–489. https://doi.org/10.1016/j.jpowsour.2007.04.018.

Kim, J., Mallarapu, A., Finegan, D.P., Santhanagopalan, S., 2021. Modeling cell venting and gas-phase reactions in 18650 lithium ion batteries during thermal runaway. J. Power Sources 489, 229496. https://doi.org/10.1016/j.jpowsour.2021.229496.

Lammer, M., Königseder, A., Hacker, V., 2017. Holistic methodology for characterisation of the thermally induced failure of commercially available 18650 lithium ion cells. RSC Adv. 7, 24425–24429. https://doi.org/10.1039/C7RA02635H.

Li, Z., Chen, L., Yan, H., Fang, Q., Zhang, Y., Xiang, H., Liu, Y., Wang, S., 2021. Gas explosions of methane-air mixtures in a large-scale tube. Fuel 285, 119239. https://doi.org/10.1016/j.fuel.2020.119239.

Lian, T., Vie, P.J.S., Gilljam, M., Forseth, S., 2019. Changes in thermal stability of cyclic aged commercial lithium-ion cells. ECS Trans. 89, 73–81. https://doi.org/10.1149/08901.0073ecst.

McBride, B.J., Gordon, S., Reno, M.A., 1993. Coefficients for Calculating Thermodynamic and Transport Properties of Individual Species (Technical No. NASA TM-4513). NASA.

Middha, P., Hansen, O.R., Groethe, M., Arntzen, B.J., 2007. Hydrogen Explosion Study in a Confined Tube: FLACS CFD Simulations and Experiments 6.

Mikolajczak, C., Kahn, M., White, K., Long, R.T., 2011. Lithium-Ion Batteries Hazard and Use Assessment. Springer US, Boston, MA. https://doi.org/10.1007/978-1-4614-3486-3.

Model Evaluation Group Gas Explosion, 1996. Gas Explosion Model Evaluation Protocol. No. Version 1.

Nedjalkov, A., Meyer, J., Köhring, M., Doering, A., Angelmahr, M., Dahle, S., Sander, A., Fischer, A., Schade, W., 2016. Toxic gas emissions from damaged lithium ion batteries—analysis and safety enhancement solution. Batteries 2, 5. https://doi.org/10.3390/batteries2010005.

Oran, E.S., Gamezo, V.N., 2007. Origins of the deflagration-to-detonation transition in gas-phase combustion. Combust. Flame 148, 4–47. https://doi.org/10.1016/j.combustflame.2006.07.010.

Peters, N., 1988. Laminar flamelet concepts in turbulent combustion. Symp. (Int.) Combust. 21, 1231–1250. https://doi.org/10.1016/S0082-0784(88)80355-2.

Roth, E.P., Crafts, C.C., Doughty, D.H., McBreen, James, 2004. Advanced Technology Development Program for Lithium-Ion Batteries : Thermal Abuse Performance of 18650 Li-Ion Cells. https://doi.org/10.2172/918751. No. SAND2004- 0584, 918751.

Savitzky, A., Golay, M.J.E., 1964. Smoothing and differentiation of data by simplified least squares procedures. Anal. Chem. 36, 1627–1639. https://doi.org/10.1021/ac60214a047.

Shen, R., Jiao, Z., Parker, T., Sun, Y., Wang, Q., 2020. Recent application of Computational Fluid Dynamics (CFD) in process safety and loss prevention: a review. J. Loss Prev. Process. Ind. 67, 104252. https://doi.org/10.1016/j.jlp.2020.104252.

Somandepalli, V., Marr, K., Horn, Q., 2014. Quantification of combustion hazards of thermal runaway failures in lithium-ion batteries. SAE Int. J. Alternative Powertrains 3, 98–104. https://doi.org/10.4271/2014-01-1857.

Srinivasan, R., Thomas, M.E., Airola, M.B., Carkhuff, B.G., Frizzell-Makowski, L.J., Alkandry, H., Reuster, J.G., Oguz, H.N., Green, P.W., La Favors, J., Currano, L.J., Demirev, P.A., 2020. Preventing cell-to-cell propagation of thermal runaway in lithium-ion batteries. J. Electrochem. Soc. 167, 020559 https://doi.org/10.1149/1945-7111/ab6ff0.

Sutherland, W., 1893. LII. *The viscosity of gases and molecular force*. Lond. Edinbur. Dublin Philosoph. Mag. J. Sci. 36, 507–531. https://doi.org/10.1080/14786449308620508.

Ben Turner, 2020. Live updates as fire rips through Carnegie Road electrical unit [WWW Document]. Liverp. Echo. URL. https://www.liverpoolecho.co.uk/news/liverpool-news/live-updates-fire-rips-through-18934842.

Wang, Q., Mao, B., Stoliarov, S.I., Sun, J., 2019. A review of lithium ion battery failure mechanisms and fire prevention strategies. Prog. Energy Combust. Sci. 73, 95–131. https://doi.org/10.1016/j.pecs.2019.03.002.

Weller, H.G., Marooney, C.J., Gosman, A.D., 1991. A new spectral method for calculation of the time-varying area of a laminar flame in homogeneous turbulence. Symp. (Int.) Combust. 23, 629–636. https://doi.org/10.1016/S0082-0784(06)80310-3.

Weller, H.G., Tabor, G., Gosman, A.D., Fureby, C., 1998. Application of a flame-wrinkling les combustion model to a turbulent mixing layer. Symp. (Int.) Combust. 27, 899–907. https://doi.org/10.1016/S0082-0784(98)80487-6.

Weller, H.G., Tabor, G., Jasak, H., Fureby, C., 1998. A tensorial approach to computational continuum mechanics using object-oriented techniques. Comput. Phys. 12, 620. https://doi.org/10.1063/1.168744.

Yoshizawa, A., 1986. Statistical theory for compressible turbulent shear flows, with the application to subgrid modeling. Phys. Fluids 29, 2152. https://doi.org/10.1063/1.865552.